UPPSALA
UNIVERSITET

Atmospheric sound propagation over large-scale irregular terrain

Martin Almquist

Project in Computational Science: Report

January 2012

PROJECT REPORT

Institutionen för informationsteknologi

Abstract

Fourth-order accurate finite difference methods have been applied to a benchmark problem on atmospheric sound propagation over irregular terrain, using the SBP-SAT method. Strict stability is shown for the acoustic wave equation with general boundary conditions in curvilinear coordinates.

Key words: high-order finite difference methods, wave propagation, numerical stability

1 Introduction

Wave propagation problems arise in many applications, such as general relativity, seismology, acoustics and electromagnetics. It can be shown that high-order (higher than second order) spatially accurate finite difference schemes combined with high-order accurate time marching schemes are well suited for such problems. It is also desirable to use schemes which do not allow non-physical growth in time, a property called strict stability. The combination of high-order accurate narrow-stencil summation-by-parts (SBP) operators and the Simultaneous Approximation Term (SAT) method for imposing the physical boundary and interface conditions is here referred to as the SBP-SAT method. The SBP-SAT method makes it possible to derive an energy estimate for the discretized model which exactly mimics the continuous energy estimate, and thus proves strict stability.

For wave propagation problems in general, the computational domain is often large compared to the wavelengths, which means that a large number of grid points is required. Thus, wave propagation problems can be computationally demanding. It is therefore desirable to use parallel computing.

We have implemented tools, based on a fourth-order accurate SBP-SAT method, for solving acoustic wave propagation problems in two spatial dimensions. The code runs in parallel in MATLAB.

In the present study we focus on the following:

1. Showing strict stability for a model problem with general boundary conditions on a curvilinear grid.

2. Validating our methods against a published benchmark problem [5], simulating acoustic sound propagation over irregular terrain.

In Section 2 we introduce some definitions and show the SBP-SAT method for the 1-D case. In Section 3 we analyze a model problem in 2-D. The results from the benchmark problem are presented in Section 4. Conclusions and ideas for future work are presented in Section 5.

2 The 1-D problem

Let the inner product for real-valued functions $u, v \in L^2[0,1]$ be defined by $(u,v) = \int_0^1 u\, v\, a(x)\, dx$, $a(x) > 0$, and let the corresponding norm be $\|u\|_a^2 = (u,u)$. The domain $(0 \le x \le 1)$ is discretized using the following $N+1$ equidistant grid points:

$$x_i = i\, h, \quad i = 0, 1, \ldots, N, \quad h = \tfrac{1}{N}\ .$$

The approximate solution at grid point x_i is denoted v_i, and the discrete solution vector is $v^T = [v_0, v_1, \ldots, v_N]$. Similarly, we define an inner product for discrete real-valued vector functions $u, v \in \mathbf{R^{N+1}}$ by $(u,v)_{H_a} = u^T\, HA\, v$, where H is diagonal and positive definite and A is the projection of $a(x)$ onto the diagonal. The corresponding norm is $\|v\|_{H_a}^2 = v^T\, HA\, v$.

Remark The matrix product HA defines a norm if and only if HA is symmetric and positive definite. This can only be guaranteed if H is a diagonal matrix (see [7] for a detailed study on this).

The following vectors will be frequently used:

$$e_0 = [1, 0, \ldots, 0]^T, \quad e_N = [0, \ldots, 0, 1]^T\ . \tag{1}$$

2.1 The SBP-SAT method

To define the SBP-SAT method, we present the following three definitions (first stated in [4] and [2]):

Definition 2.1 *An explicit pth-order accurate finite difference scheme with minimal stencil width of a Cauchy problem is called a pth-order accurate narrow-stencil.*

Definition 2.2 *A difference operator $D_1 = H^{-1}Q$ approximating $\partial/\partial\, x$, using a pth-order accurate narrow-stencil, is said to be a pth-order accurate narrow-diagonal first-derivative SBP operator if H is diagonal and positive definite and $Q + Q^T = diag\,(-1, 0, \ldots, 0, 1)$.*

Definition 2.3 *Let $D_2^{(b)} = H^{-1}(-M^{(b)} + \bar{B}S)$ approximate $\partial/\partial\, x\,(\, b\, \partial/\partial\, x)$, where $b(x) > 0$, using a pth-order accurate narrow-stencil. $D_2^{(b)}$ is said to be a pth-order accurate narrow-diagonal second-derivative SBP operator, if H is diagonal and positive definite, $M^{(b)}$ is symmetric and positive semi-definite, S approximates the first-derivative operator at the boundaries and $\bar{B} = diag\,(-b_0, 0 \ldots, 0, b_N)$.*

We say that a scheme is explicit if no linear system of equations needs to be solved to compute the difference approximation.

As an example of the simple, yet powerful, SBP-SAT method, we consider the following second-order hyperbolic equation:

$$\begin{array}{llll} au_{tt} = (bu_x)_x, & & 0 \le x \le 1, & t \ge 0, \\ \alpha u_t - bu_x = g, & & x = 0, & t \ge 0, \\ \alpha u_t + bu_x = g, & & x = 1, & t \ge 0, \\ u = f_1, & u_t = f_2, & 0 \le x \le 1, & t = 0, \end{array} \tag{2}$$

where $a(x) > 0$ and $b(x) > 0$. Multiplying the first equation in (2) by u_t, integrating by parts (referred to as "the energy method") and imposing the boundary conditions leads to

$$\frac{d}{dt}\left(\|u_t\|_a^2 + \|u_x\|_b^2\right) = -2\left(\alpha u_t - g\right)u_t|^{x=1} - 2\left(\alpha u_t - g\right)u_t|_{x=0} \,. \tag{3}$$

An energy estimate is obtained if $\alpha \ge 0$. The discrete approximation of (2) using the SBP-SAT method is

$$\begin{array}{ll} Av_{tt} = D_2^{(b)}v & -H^{-1}\tau e_0\left\{(\alpha v_t - BSv)_0 - g\right\} \\ & -H^{-1}\tau e_N\left\{(\alpha v_t + BSv)_N - g\right\} \,. \end{array} \tag{4}$$

where e_0 and e_N are defined in (1). (We assume the same initial conditions $v = f_1, \quad v_t = f_2$ as in the continuous case). The matrices A and B have the values of $a(x)$ and $b(x)$ injected on the diagonal.

Applying the energy method by multiplying (4) by $v_t^T H$ and adding the transpose leads to

$$\begin{array}{ll} \frac{d}{dt}\left(\|v_t\|_{H_a}^2 + v^T M^{(b)} v\right) = & -(v_t^T)_0\left(2 - 2\tau\right)(BSv)_0 + (v_t^T)_N\left(2 - 2\tau\right)(BSv)_N \\ & +2\tau\left(v_t^T(g - \alpha v_t)\right)_0 + 2\tau\left(v_t^T(g - \alpha v_t)\right)_N \,. \end{array}$$

Setting $\tau = 1$ leads to

$$\frac{d}{dt}\left(\|v_t\|_{H_a}^2 + v^T M^{(b)} v\right) = -2\left(v_t^T(\alpha v_t - g)\right)_0 - 2\left(v_t^T(\alpha v_t - g)\right)_N \,. \tag{5}$$

Equation (5) is a semi-discrete analogue to (3).

3 Analysis in 2D

In this section we analyze the scalar 2-D wave equation with general boundary conditions. To allow for complex domains, we transform the equation given on a curvilinear domain to an equation on a rectangular domain. We then derive an energy estimate for the continuous case. After discretizing the model in space with the SBP-SAT method, we prove strict stability by exactly mimicking the continuous energy estimate in the semi-discrete case.

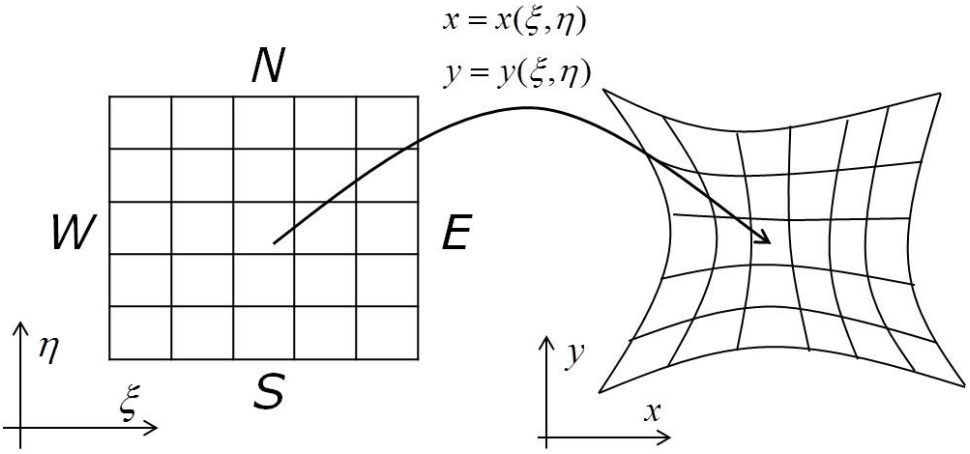

Figure 1: The mapping between cartesian (left) and curvilinear (right) coordinates.

3.1 Definitions

If the problem is given on a curvilinear domain Ω, we transform it to the unit square, Ω'. We will refer to Ω as the physcial domain and Ω' as the logical domain. The logical domain is discretized using the $(N_\xi + 1)(N_\eta + 1)$ grid points:

$$(\xi_i, \eta_j) = \left(\frac{i}{N_\xi}, \frac{j}{N_\eta} \right), \qquad i = 0, 1, ..., N_\xi, \quad j = 0, 1, ..., N_\eta.$$

The boundaries of Ω' are denoted by W (west), N (north), E (east) and S (south), respectively, as shown in Figure 1. The approximate solution at a grid point (ξ_i, η_j) is denoted by v_{ij}, and the discrete solution vector is $v^T = [v_{00}, ..., v_{0N_\eta}, v_{10}, ..., v_{N_\xi N_\eta}]$. The matrix i_W is defined so that $i_W v$ is a vector with the same length as v and the same elements on the positions corresponding to the west boundary, but zeros everywhere else. The matrices i_N, i_E and i_S are defined similarly for the north, east and south boundaries, respectively.

By $D_{1\xi}$ we denote the 2-D version of the narrow-stencil first-derivative SBP operator D_1, approximating $\frac{\partial}{\partial \xi}$. Similarly, $D_{2\xi}^{(b)}$ approximates $\frac{\partial}{\partial \xi}\left(b \frac{\partial}{\partial \xi}\right)$. In the same manner, we let H_ξ denote the 2-D version of the diagonal matrix H, applied in the ξ-direction.

3.2 The continuous problem

We consider the following problem:

$$\begin{array}{lll} u_{tt} = (bu_x)_x + (bu_y)_y & (x,y) \in \Omega, & t \geq 0 \\ \gamma_1 u + \gamma_2 b \nabla u \cdot \mathbf{n} + \gamma_3 u_t = 0 & (x,y) \in \partial\Omega, & t \geq 0 \\ u = f_1, \quad u_t = f_2, & (x,y) \in \Omega, & t = 0, \end{array} \tag{6}$$

where $b(x,y) > 0$. We have chosen homogeneous boundary conditions to avoid unnecessary notation in the analysis, but the analysis holds for inhomogeneous conditions as well. We also limit our present study to the case $\gamma_2 \neq 0$, which includes the important case of Neumann conditions ($\gamma_1 = 0, \gamma_2 = 1, \gamma_3 = 0$).

Remark Dirichlet conditions ($\gamma_1 = 1, \gamma_2 = \gamma_3 = 0$) form an important category of boundary conditions which are not included in the case $\gamma_2 \neq 0$. Treating Dirichlet conditions with the SAT method is more complicated than treating the conditions of the present study. For a detailed analysis of this matter see for example [3]. However, it can be shown that imposing Dirichlet conditions *strongly* also results in a strictly stable scheme.

Assume that there is a smooth one-to-one mapping

$$\begin{cases} x = x(\xi, \eta) \\ y = y(\xi, \eta), \end{cases}$$

from Ω' to Ω. The Jacobian J of the transformation is

$$J = x_\xi y_\eta - x_\eta y_\xi.$$

The *scale factors* η_1 and η_2 of the transformation are defined as

$$\eta_1 = \sqrt{x_\xi^2 + y_\xi^2}, \quad \eta_2 = \sqrt{x_\eta^2 + y_\eta^2}. \tag{7}$$

Since the mapping is one-to-one, the Jacobian is everywhere non-zero. By the chain rule, we have

$$\begin{cases} u_\xi = u_x x_\xi + u_y y_\xi \\ u_\eta = u_x x_\eta + u_y y_\eta, \end{cases}$$

which is equivalent to

$$\begin{cases} u_x = \frac{1}{J}\left(u_\xi y_\eta - u_\eta y_\xi\right) = \frac{1}{J}\left((u y_\eta)_\xi - (u y_\xi)_\eta\right) \\ u_y = \frac{1}{J}\left(u_\eta x_\xi - u_\xi x_\eta\right) = \frac{1}{J}\left((u x_\xi)_\eta - (u x_\eta)_\xi\right). \end{cases} \tag{8}$$

Replacing u with bu_x and bu_y in (8) yields

$$\begin{aligned} (bu_x)_x &= \tfrac{1}{J}\left(\tfrac{b}{J}\left(u_\xi y_\eta - u_\eta y_\xi\right) y_\eta\right)_\xi - \tfrac{1}{J}\left(\tfrac{b}{J}\left(u_\xi y_\eta - u_\eta y_\xi\right) y_\xi\right)_\eta \\ (bu_y)_y &= \tfrac{1}{J}\left(\tfrac{b}{J}\left(u_\xi x_\eta - u_\eta x_\xi\right) x_\eta\right)_\xi - \tfrac{1}{J}\left(\tfrac{b}{J}\left(u_\xi x_\eta - u_\eta x_\xi\right) x_\xi\right)_\eta. \end{aligned} \tag{9}$$

By adding $(bu_x)_x$ and $(bu_y)_y$ and rearranging terms, the first equation in (6) can be written as

$$Ju_{tt} = (\alpha_1 u_\xi)_\xi + (\beta u_\xi)_\eta + (\beta u_\eta)_\xi + (\alpha_2 u_\eta)_\eta, \quad (\xi, \eta) \in \Omega' \tag{10}$$

where

$$\alpha_1 = \frac{b}{J}\left(y_\eta^2 + x_\eta^2\right), \beta = -\frac{b}{J}\left(y_\eta y_\xi + x_\eta x_\xi\right), \alpha_2 = \frac{b}{J}\left(y_\xi^2 + x_\xi^2\right).$$

Using equation (8) to transform $\nabla u \cdot \mathbf{n}$ in the second equation in (6) yields the transformed boundary condition:

$$\begin{cases} \gamma_1\eta_2 u - \gamma_2\left(\alpha_1 u_\xi + \beta u_\eta\right) + \gamma_3\eta_2 u_t = 0, & (\xi, \eta) \in W \\ \gamma_1\eta_2 u + \gamma_2\left(\alpha_1 u_\xi + \beta u_\eta\right) + \gamma_3\eta_2 u_t = 0, & (\xi, \eta) \in E \\ \gamma_1\eta_1 u - \gamma_2\left(\alpha_2 u_\eta + \beta u_\xi\right) + \gamma_3\eta_1 u_t = 0, & (\xi, \eta) \in S \\ \gamma_1\eta_1 u + \gamma_2\left(\alpha_2 u_\eta + \beta u_\xi\right) + \gamma_3\eta_1 u_t = 0, & (\xi, \eta) \in N. \end{cases} \tag{11}$$

The complete transformed problem is given by (10), (11) and the initial conditions stated in (6). Applying the energy method leads to

$$\frac{d}{dt}E = -\int_W \frac{\gamma_3}{\gamma_2}\eta_2 u_t^2 dr - \int_E \frac{\gamma_3}{\gamma_2}\eta_2 u_t^2 dr - \int_N \frac{\gamma_3}{\gamma_2}\eta_1 u_t^2 dr - \int_S \frac{\gamma_3}{\gamma_2}\eta_1 u_t^2 dr \tag{12}$$

where

$$E = \frac{1}{2}\left(\int_{\Omega'} J u_t^2 d\Omega' + \int_{\Omega'} \begin{bmatrix} u_\xi & u_\eta \end{bmatrix} \begin{bmatrix} \alpha_1 & \beta \\ \beta & \alpha_2 \end{bmatrix} \begin{bmatrix} u_\xi u_\eta \end{bmatrix} d\Omega' + BT\right) \tag{13}$$

and

$$BT = \int_W \frac{\gamma_1}{\gamma_2}\eta_2 u^2 dr + \int_E \frac{\gamma_1}{\gamma_2}\eta_2 u^2 dr + \int_N \frac{\gamma_1}{\gamma_2}\eta_1 u^2 dr + \int_S \frac{\gamma_1}{\gamma_2}\eta_1 u^2 dr. \tag{14}$$

The matrix $\begin{bmatrix} \alpha_1 & \beta \\ \beta & \alpha_2 \end{bmatrix}$ is positive definite since $\alpha_1 > 0$ and $\alpha_1\alpha_2 - \beta^2 = (x_\xi y_\eta - x_\eta y_\xi)^2 = J^2 > 0$. Thus, the problem has an energy estimate if the relations

$$\frac{\gamma_1}{\gamma_2} \geq 0, \quad \frac{\gamma_3}{\gamma_2} \geq 0 \tag{15}$$

hold.

3.3 The semi-discrete problem

The discrete version of (11) is given by

$$\begin{cases} L^W v = i_W\left\{\gamma_1\eta_2 v + \gamma_2\left(\bar{B}^{(\alpha_1)} S_\xi v - \beta D_{1\eta} v\right) + \gamma_3\eta_2 v_t\right\} = 0 \\ L^E v = i_E\left\{\gamma_1\eta_2 v + \gamma_2\left(\bar{B}^{(\alpha_1)} S_\xi v + \beta D_{1\eta} v\right) + \gamma_3\eta_2 v_t\right\} = 0 \\ L^S v = i_S\left\{\gamma_1\eta_1 v + \gamma_2\left(\bar{B}^{(\alpha_2)} S_\eta v - \beta D_{1\xi} v\right) + \gamma_3\eta_1 v_t\right\} = 0 \\ L^N v = i_N\left\{\gamma_1\eta_1 v + \gamma_2\left(\bar{B}^{(\alpha_2)} S_\eta v + \beta D_{1\xi} v\right) + \gamma_3\eta_1 v_t\right\} = 0. \end{cases} \tag{16}$$

The semi-discrete approximation of (10) and (11) using the SBP-SAT method is

$$\begin{aligned} Jv_{tt} = & D_{2\xi}^{(\alpha_1)}v + D_{1\xi}\beta D_{1\eta}v + D_{1\eta}\beta D_{1\xi}v + D_{2\eta}^{(\alpha_2)}v \\ & + \tau_1 H_\xi^{-1}L^W v + \tau_1 H_\xi^{-1}L^E v + \tau_2 H_\eta^{-1}L^S v + \tau_2 H_\eta^{-1}L^N v. \end{aligned} \tag{17}$$

One of the main results of the present study is stated in the following lemma:

Lemma 3.1 *The scheme (17) is strictly stable if* $\tau_1 = \tau_2 = -\frac{1}{\gamma_2}$ *and the conditions (15) hold.*

Proof Applying the energy method by multiplying (17) by $v_t^T H_\xi H_\eta$ and adding the transpose leads to

$$\begin{aligned} \tfrac{d}{dt}E = \; & (1+\tau_1\gamma_2)v_t^T H_\eta \bar{B}^{(\alpha_1)} S_\xi v + (1+\tau_2\gamma_2)v_t^T H_\xi \bar{B}^{(\alpha_2)} S_\eta v \quad + \\ & (1+\tau_1\gamma_2)\, v_t^T H_\eta \left(-i_W + i_E\right)\beta D_{1\eta}v \quad + \\ & (1+\tau_2\gamma_2)\, v_t^T H_\xi \left(-i_S + i_N\right)\beta D_{1\xi}v \quad + \\ & \tau_1\gamma_3 v_t^T H_\eta \eta_2 \left(i_W + i_E\right) v_t + \tau_2\gamma_3 v_t^T H_\xi \eta_1 \left(i_S + i_N\right) v_t, \end{aligned}$$

where

$$\begin{aligned} E = \; & \tfrac{1}{2} v_t^T H_\xi H_\eta J v_t \quad + \\ & \tfrac{1}{2}\left(v^T H_\eta M_\xi^{(\alpha_1)} v + v^T H_\xi M_\eta^{(\alpha_2)} v + 2\left(D_{1\xi}v\right)^T \beta H_\xi H_\eta \left(D_{1\eta}v\right)\right) + \\ & \tfrac{1}{2}\left(-\tau_1\gamma_1 v^T H_\eta \eta_2 (i_W + i_E)v - \tau_2\gamma_1 v^T H_\xi \eta_1 (i_S + i_N)v\right). \end{aligned}$$

By choosing $\tau_1 = \tau_2 = -\frac{1}{\gamma_2}$ we obtain an energy estimate completely analogous to (12). If (15) holds, we have a non-growing energy. □

4 Application: Atmospheric sound propagation over irregular terrain

4.1 The model

We consider sound propagation over the terrain shown in Figure 2. A source which emits spherical waves with a frequency of 50 Hz is placed at $r = 0$ at a height of 10 m. The sound speed is constant at 340 m/s.

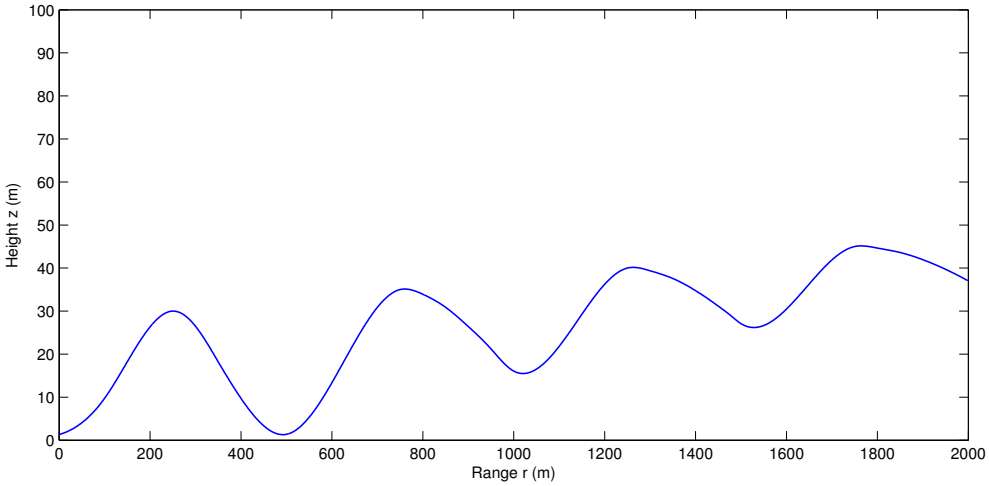

Figure 2: The topology (solid line).

The propagation of sound waves is governed by the acoustic wave equation

$$u_{tt} = \nabla \cdot (b \nabla u), \tag{18}$$

where u is the acoustic pressure and b is the square of the wave velocity. Expressing equation (18) in cylindrical coordinates (r, ϕ, z) and assuming symmetry in the azimuthal direction (the ϕ-direction) results in the axisymmetric two-dimensional restriction of (18),

$$u_{tt} = \frac{1}{r}\frac{\partial}{\partial r}\left(rb\frac{\partial u}{\partial r}\right) + \frac{\partial}{\partial z}\left(b\frac{\partial u}{\partial z}\right). \tag{19}$$

We construct the computational domain by introducing artificial boundaries as shown in Figure 3. The dot marks the location of the source, just outside the west boundary of the computational domain.

The boundary condition at the south boundary is given by (see [5])

$$\left(\frac{\tilde{a}\omega_0}{c} - \frac{\chi}{2}\right) u + \nabla u \cdot \mathbf{n} + \frac{\tilde{b}}{c} u_t = 0, \tag{20}$$

where c is the wave speed, $\mathbf{n}$ is the unit outward normal, ω_0 is the angular frequency, χ is the curvature and $\tilde{a}$ and $\tilde{b}$ satisfy the relation

$$\tilde{a} + \tilde{b}i = \frac{i}{\hat{Z}}, \tag{21}$$

where $\hat{Z}$ is the normalized sound impedance, $\hat{Z} = 18.3 + 17.5i$. The curvature χ is defined as

$$\chi(r) = \frac{-H_{rr}(r)}{(1 + H_r^2(r))^{3/2}}, \tag{22}$$

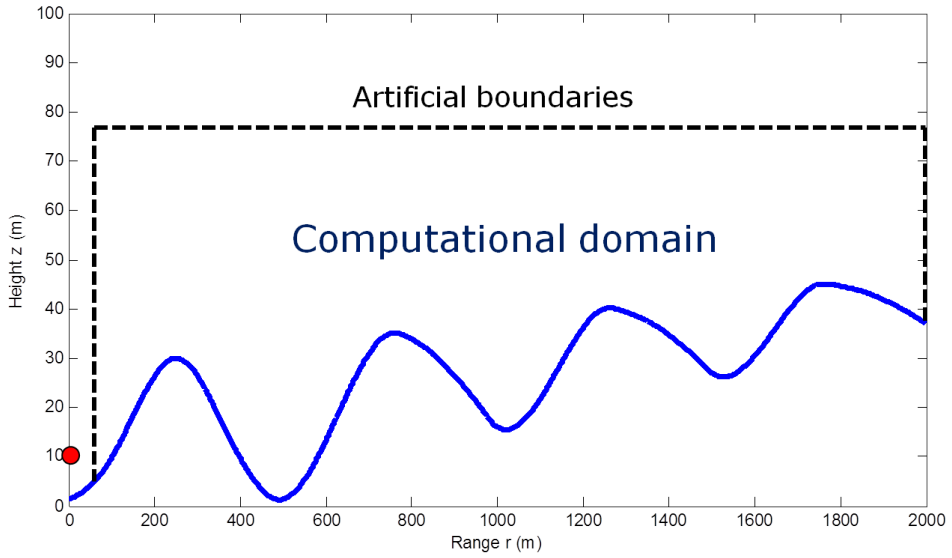

Figure 3: The computational domain. The dot at the z-axis represents the point source.

where $H(r)$ denotes the height of the ground at horizontal position r.

The north and east boundaries are introduced to truncate the domain. We want to avoid non-physical reflections at these boundaries. To that end, we apply first order Engquist Majda absorbing boundary conditions [1], given by

$$u_t + \sqrt{b}\nabla u \cdot \hat{\mathbf{n}} = 0. \tag{23}$$

This boundary condition is perfectly absorbing at normal incidence. For a 45° incidence, a wave with an amplitude that equals 17% of the amplitude of the incident wave is reflected. Close to glancing, the reflection coefficient tends to unity.

At the west boundary, the boundary condition is determined by the source. Consider a point source with amplitude A and frequency f. At a distance $\tilde{r}$ from the source, the acoustic pressure is given by

$$u(\tilde{r}, t) = \frac{A}{\tilde{r}} \sin\left(2\pi f\left(t - \frac{\tilde{r}}{c}\right)\right). \tag{24}$$

Now let the source be located at $(r, z) = (0, z_0)$. The distance $\tilde{r}$ from the source to the vertical boundary ($(r, z) = (r_B, z), \quad z \geq H(r_B)$) is given by

$$\tilde{r} = \sqrt{r_B^2 + (z - z_0)^2}. \tag{25}$$

Combining (24) and (25) yields

$$u(r_B, z, t) = \frac{A}{\sqrt{r_B^2 + (z - z_0)^2}} \sin\left(2\pi f\left(t - \frac{\sqrt{r_B^2 + (z - z_0)^2}}{c}\right)\right), \quad (26)$$

which is the Dirichlet boundary condition on the west boundary. The right hand side can be thought of as a forcing function that drives the waves emitted by the source through the west boundary and into the computational domain.

We now introduce logical coordinates (ξ, η) and perform *orthogonal* transformations from the unit square $(0 <= \xi <= 1, 0 <= \eta <= 1)$ onto the physical domain $(r(\xi, \eta), z(\xi, \eta)) \in \Omega$. Under such transformations, equation (19) becomes (see [6])

$$r\eta_1\eta_2 u_{tt} = \left(rb\frac{\eta_2}{\eta_1}u_\xi\right)_\xi + \left(rb\frac{\eta_1}{\eta_2}u_\eta\right)_\eta, \quad (\xi, \eta) \in \Omega', \quad (27)$$

where η_1 and η_2 are the scale factors of the transformation, defined in (7). Noting that under an orthogonal transformation the Jacobian J of the transformation is related to the scale factors as $J = \eta_1\eta_2$ and defining the coefficients $\tilde{\alpha}_1$ and $\tilde{\alpha}_2$ as

$$\tilde{\alpha}_1 = rb\frac{\eta_2}{\eta_1}, \quad \tilde{\alpha}_2 = rb\frac{\eta_1}{\eta_2}, \quad (28)$$

we can rewrite (27) as

$$rJu_{tt} = (\tilde{\alpha}_1 u_\xi)_\xi + (\tilde{\alpha}_2 u_\eta)_\eta, \quad (\xi, \eta) \in \Omega' \quad (29)$$

or, with $\tilde{J} = rJ$,

$$\tilde{J}u_{tt} = (\tilde{\alpha}_1 u_\xi)_\xi + (\tilde{\alpha}_2 u_\eta)_\eta, \quad (\xi, \eta) \in \Omega'. \quad (30)$$

Remark Our numerical method is not limited to orthogonal mappings, but we chose to use an orthogonal mapping in this case because it simplifies the analysis and the implementation somewhat. Note that equation (30) has the same form as equation (10). The coefficients β corresponding to the mixed derivatives are zero because orthogonality was assumed. Thus, (30) is a special case of (10).

The model that we solve is the equation (30) with the boundary conditions (20), (23) and (26). The boundary conditions (20) and (23) are of the type thoroughly analyzed in Section 3. The west boundary condition (26) is a Dirichlet boundary condition and can be imposed strongly as mentioned in Section 3. Thus, the analysis performed in Section 3, proving well-posedness for the continuous problem and strict stability for the discrete scheme, holds for this model too.

4.2 Grid generation

To apply the fourth-order accurate finite difference method, a computational grid must be constructed in the physical domain. Generating a good grid on a complex domain is not a trivial task. If the computational grid is not smooth enough, the order of accuracy of the method will decrease. We have installed and used Pointwise, a commercial software for creating large grids. After creating a grid with Pointwise, its quality can be enhanced by letting Pointwise apply elliptic smoothing in an interative process. The smoothing can be altered in different ways according to the needs of the user. In this problem, the grid was required to be orthogonal, since the transformation was assumed to be orthogonal. Orthogonality was therefore given high priority in the smoothing process. Figure 4 shows an example of a coarse grid. Note that the grid is stretched in the vertical direction. Since we are interested in the solution close to the ground we want high accuracy in that region, but far from the ground we can afford to lose some accuracy in order to reduce the number of grid points. Table 1 lists the total number of gridpoints required when using 6,12 and 24 points per acoustic wavelength close to the ground, with the north boundary at a height of 400 m.

Resolution (points per wavelength)	N_r	N_z	$N_r \cdot N_z$
6	1766	201	354966
12	3531	401	1415931
24	7061	801	5655861

Table 1: Number of grid points corresponding to different resolutions close to the south boundary. North boundary at $z = 400$ m.

4.3 Simulations

We have implemented a parallel solver using a fourth-order accurate SBP-SAT method of the benchmark model and fourth-order Runge-Kutta for discretization in time. The solver was implemented in parallel in MATLAB, using MATLAB's Parallel Computing toolbox. To further increase the performance of the code, MEX-files based on C code were used for performing the bulk of the computations. MEX-files are dynamically linked subroutines produced from C, C++ or Fortran source code that can be run from within MATLAB. All the simulations were performed on an HP Z400 Workstation with six Intel Xeon 64 bit 3.33 GHz CPUs.

In the simulations, we marched in time until the solution reached steady state and then computed the amplitude of the sound waves by measuring $|v|_{max}$, the maximum absolute value of the solution during one period. The

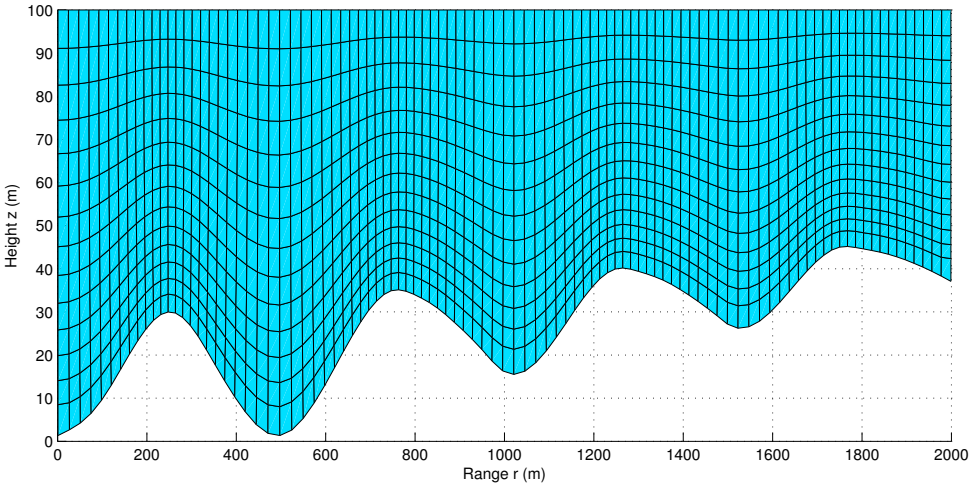

Figure 4: Coarse example grid. The grid looks very unorthogonal because of the different length scales of the axes.

propagation loss P (measured in dB) was computed as

$$P = -20\log\left(\frac{|v|_{max}}{A}\right), \tag{31}$$

where A is the amplitude of point source. Specifically, we studied the propagation loss 1 m above the ground. In this context, it is not obvious where the artificial boundaries should be placed. Considering that we are mostly interested in the solution at 1 m above the ground, where should we place the north boundary? The lower we can place it, the smaller our computational domain becomes, and the faster we can solve the problem. However, since the absorbing boundary condition used is not completely absorbing, we know that we will get unwanted reflections off the north boundary. The higher we place it, the smaller these reflected waves will be as they reach the area of interest close to the ground, as they will have traveled a longer distance from the source *and* reached the north boundary with and angle of incidence closer to 90°, which is where the absorbing boundary condition is most efficient. To improve the accuracy of the model, we need to place the north boundary high enough that the waves that reach the ground after having been reflected off the north boundary are insignificant compared to the "true" waves at ground level. An alternative solution could be to use more efficient absorbing boundary conditions.

To verify the SBP-SAT method, we performed a convergence study with the north boundary at a height of 400 m. Figure 5 shows the propagation loss obtained using the grids described in Table 1. As we can see, the curves corresponding to 12 and 24 points per wavelength are almost identical. This

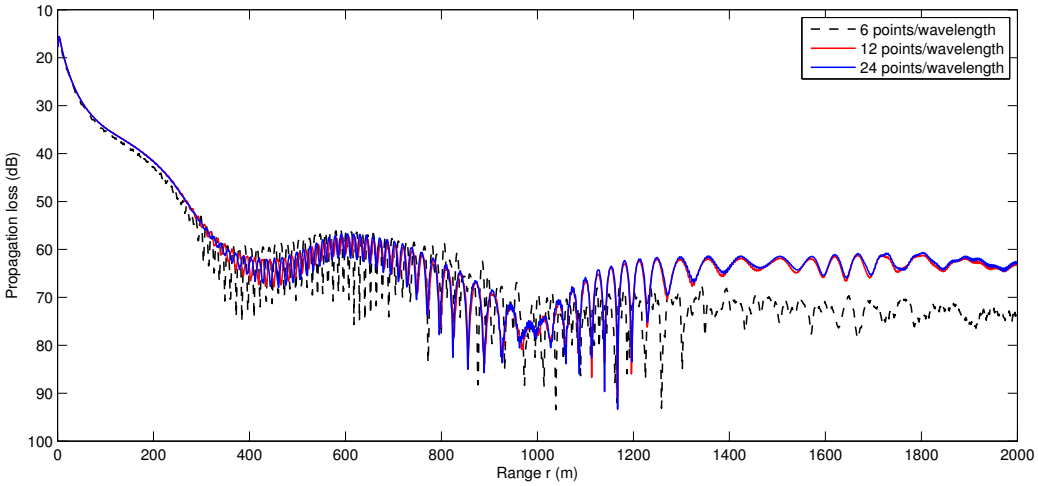

Figure 5: Convergence study with the north boundary at a height of 400 m.

proves convergence. We can also see that the curve obtained using 6 grid points per wavelength is very far from the others, which proves that finer grids have to be used in order to solve this problem accurately. In the remaining simulations, grids with 14 points per wavelength close to the south boundary were used.

In order to find a suitable height for the north boundary, we computed the propagation loss for four different heights of the north boundary. The results are compared in Figure 6. Since the curves are very different, we can conclude that reflections off the north boundary can have a large impact on the solution. Notice the large oscillations caused by reflections from the north boundary. As the boundary is raised, the region with oscillations moves to the right. With the boundary at 2000 m, no large oscillations appear on the curve. We can also see that the curves seem to converge. The curves obtained with the boundary at 1000 m and 2000 m are very similar except for the large oscillations that appear on the 1000 m curve, about 1200 m from the source. This pattern indicates that the solution will not change much if we raise the boundary even higher than 2000 m.

Figure 7 shows the propagation loss measured in dB for all the points in the domain up to a height of 100 m, computed with the north boundary at $z = 2000$ m. Just like the curve in Figure 6 the contour plot is very smooth close to the source, but shows oscillatory behaviour far away, where the true sound level is low. We can see that the oscillations first appear in the valley about 1000 m from the source. This is because the true sound level in general is lower in the valleys than on the hills, and therefore more sensitive to reflections from the north boundary.

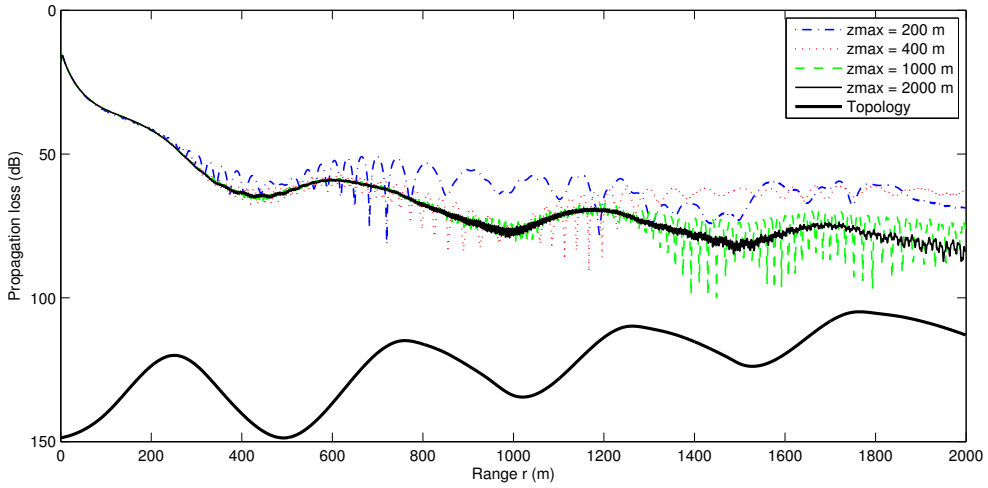

Figure 6: Propagation loss measured 1 m above ground for different locations of the north boundary.

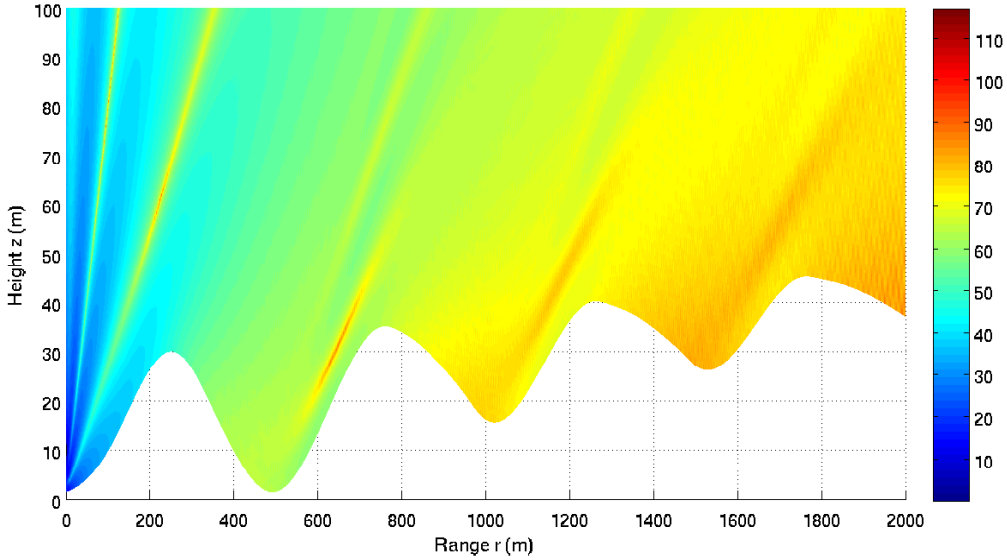

Figure 7: Propagation loss (dB) with the north boundary at $z = 2000$ m.

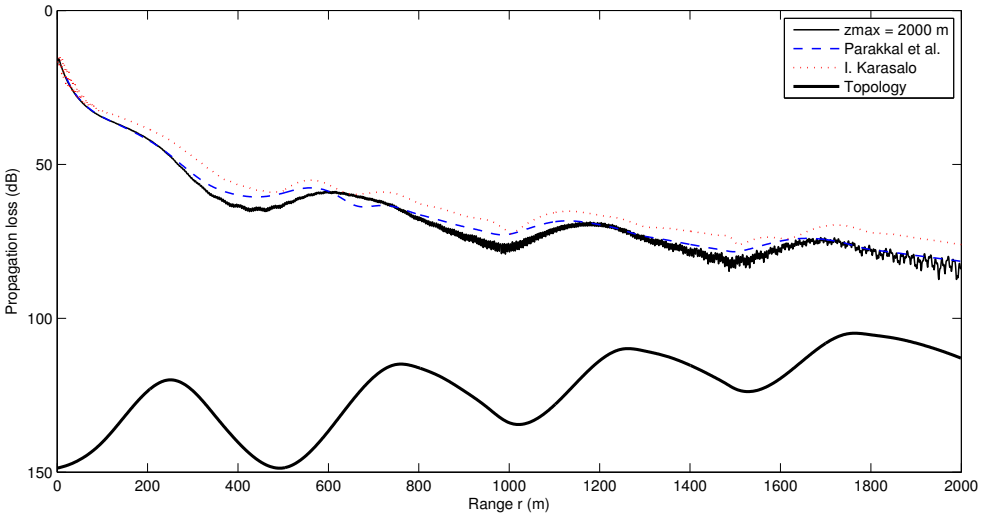

Figure 8: Comparison of results.

In Figure 8 we compare our result, obtained with the north boundary at 2000 m, with the results published in [5] and the results obtained by Ilkka Karasalo at the Swedish Defense Research Agency. Both of the other results have been obtained by solving a simplified model based on the parabolic equation approach in frequency domain. Considering that we used a completely different method, the results are actually very similar. Our result is closest to the result published in [5].

5 Conclusions and future work

In Section 4 we showed that reflections from artifical boundaries can affect the solution. To solve the problem accurately with first order Engquist Majda absorbing boundary conditions we had to place the north border very high up and thus create a large computational domain. This is a very inefficient approach from a computational point of view. In order to solve this kind of problem efficiently, we need to find a more accurate way to impose artificial boundaries. In the future, other types of more efficient absorbing boundary conditions will be studied. We will also investigate so called sponge layers where damping terms are introduced in the partial differential equation.

Acknowledgements

The author would like to thank his supervisor doctor Ken Mattsson for introducing him to the subject and for offering invaluable comments on an early draft of this report.

References

[1] B. Engquist and A. Majda. Radiation boundary conditions for acoustic and elastic wave calculations. *Comm. Pure Appl. Math.*, 32:313–357, 1979.

[2] K. Mattsson, F. Ham, and G. Iaccarino. Stable and accurate wave propagation in discontinuous media. *J. Comput. Phys.*, 227:8753–8767, 2008.

[3] K. Mattsson, F. Ham, and G. Iaccarino. Stable boundary treatment for the wave equation on second-order form. *Journal of Scientific Computing*, 41:366–383, 2009.

[4] K. Mattsson, M. Svärd, and M. Shoeybi. Stable and accurate schemes for the compressible navier-stokes equations. *J. Comput. Phys.*, 227(4):2293–2316, 2008.

[5] S. Parakkal, KE. Gilbert, D. Xiao, and HE. Bass. A generalized polar coordinate method for sound propagation over large-scale irregular terrain. *J Acoust Soc Am.*, 128(5):2573–2580, 2010.

[6] E. Sundkvist and K. Otto. Discretization of a Hybrid Model for Acoustic Wave Propagation in Layered Fluid Media. Technical report, Dep. of Information Technology, Uppsala Univ., Uppsala, Sweden, 2011.

[7] M. Svärd. On coordinate transformation for summation-by-parts operators. *Journal of Scientific Computing*, 20(1), 2004.